IOP Publishing Journal of Physics D: Applied Physics
J. Phys. D: Appl. Phys. **40** (2007) 3557–3562 doi:10.1088/0022-3727/40/12/002

Micro-imaging synchrotron–laser interactions in wide band-gap luminescent materials

N R J Poolton[1], B M Towlson[2], B Hamilton[2], J Wallinga[3] and A Lang[4]

[1] Synchrotron Radiation Department, CCLRC Daresbury Laboratory, Warrington WA4 4AD, UK
[2] Department of Electrical Engineering and Electronics, The University of Manchester, PO Box 88, Manchester M60 1QD, UK
[3] Radiation, Radionuclides and Reactors Department, Delft University of Technology, Mekelweg 15, 2629 JB Delft, The Netherlands
[4] Department of Geography, Liverpool University, Liverpool L69 7ZT, UK

E-mail: n.r.j.poolton@dl.ac.uk

Received 5 January 2007, in final form 22 April 2007
Published 4 June 2007
Online at stacks.iop.org/JPhysD/40/3557

Abstract
Rapid advances have recently been made at SRS Daresbury in optical-detection methods for both micro-imaging x-ray absorption spectroscopy (ODXAS, ODEXAFS), and in the development of volume-integrated synchrotron–laser pump–probe XAS methods (PP-ODXAS). The purpose of the present work is to describe the latest developments that enable these two methods to be coupled, providing micro-imaging of both the transient and CW synchrotron–laser interactions. Examples are provided whereby the distribution of both radiative and non-radiative centres in heterogeneous silicate samples can be mapped and directly correlated with the chemistry and structure of the host lattice.

1. Introduction

Optical detection of x-ray absorption spectroscopy (ODXAS) is an ideal method for directly linking the luminescence emission characteristics of a solid, with the chemistry and structure of the host from which it derives. The method works because the dynamics of charge transfer between the x-ray absorbing and luminescence emitting events change as the core levels of the constituent atoms are traversed. As a consequence, the EXAFS signatures are observable by luminescence intensity changes of photons being emitted within the charge migration distance from the absorbing event. Examples of the method are provided by Soderholm *et al* (1998) for luminescence involving rare earth emissions, Dalba *et al* (2000) for porous silicon, and full theoretical consideration of the method has been provided by Emura *et al* (1993). However, because the XAS/EXAFS features are carried by optical photons, this opens the possibilities for deploying optical microscopy methods for micro-imaging the processes with spatial resolutions up to the diffraction limit of the emitted photons (~200 nm in the UV), and this route has been exploited by the recent construction of a unique instrument CLASSIX (Chemistry, Luminescence And Structure of Surfaces via micro-Imaging X-ray absorption) at SRS Daresbury (Poolton *et al* 2006a). Because of the detection method, the spectrometer is portable and can be implemented on most synchrotron beamlines which provide flux in a useful energy range (typically 4 eV, continuously through to 40 keV).

Whilst OD-XAS provides a direct link between the sample chemistry, structure and radiative recombination sites, parallel knowledge about the possible presence of non-radiative defects is also of primary interest: their presence can significantly affect the luminescence efficiency of an emitting sample and for some wide-gap materials, the defects can act as important dosimetry sites capable of trapping and storing charge for extended periods of time. Unfortunately, detecting the presence of competitive non-radiative defects and analysing their properties is extremely difficult. However, the simultaneous interaction of both synchrotron and laser light provides a route to this end. Whilst the synchrotron provides

a pump for both the radiative and non-radiative recombination pathways, the presence of the latter can be directly inferred by an increase in emission resulting from recombination at the main *luminescence* centres, as charge is removed from the *non-radiative* defects. This increase can be either temporal or CW, depending on the relative capture cross-sections of the defect interaction with laser and synchrotron photons, and of the free charge. Potentially, the laser can also interact directly with the radiative recombination centres, but the dynamics of these interactions will be significantly different and usually results in quenching of the synchrotron-stimulated luminescence.

By varying the pump energy in volume-integrated measurements, a direct link between the sample chemistry/structure and the non-radiative centres is possible via such pump–probe ODXAS (PP-ODXAS) methods (Poolton *et al* 2005, 2006b). The purpose of this article is to describe how PP-ODXAS and micro-imaging ODXAS can be combined to provide a powerful method for recording the spatial variations of both radiative and non-radiative centres actively involved in luminescence processes and directly correlating them with the sample chemistry and structure.

2. Experimental details

The experiments described in this work were undertaken by combining the new spectrally resolving micro-imaging ODXAS spectrometer CLASSIX with a range of modulating solid-state laser diodes, as deployed on SRS beamline MPW6.1. Essentially, CLASSIX consists of an ultra-sensitive CCD array (single photon counting; 200–1000 nm detection: Andor Technology, iXon DV887), coupled to variable magnification UV-to-IR transmitting lenses (providing spatial resolution up to 400 nm maximum), with emission dispersed via a custom-built filter-monochromator operating in the range 200–1000 nm, at spectral resolutions of up to 10 nm. The optics collect light emitted from samples cooled to 40 K with liquid helium, located within a UHV chamber which is coupled directly to the XUV beamline. With a maximum readout rate of 10 MHz, the CCD (without pixel binning) allows transient luminescence signals to be detected with time-constants >50 ms.

MPW6.1 is a high-flux wiggler station, providing photons in the range 40–450 eV (Bowler *et al* 2002), though the experiments described here concentrate mainly on the range 270–320 eV, spanning the $L_{2,3}$ core-level transitions of potassium.

The lasers used in the study were all fibre-coupled solid-state devices, with an average power output of 50 mW, covering the energy range 1.2–3 eV (404, 445, 532, 635, 785, 830 and 985 nm); most of these are semiconductor diodes, modulating from CW up to 20 MHz whereas the 532 nm module is a frequency-doubled YAG system, modulating in a more modest range from CW to 5 kHz. The optics were arranged such that the synchrotron-pump and laser-probe footprints overlap in the interaction region of interest: the footprint of the former is typically $\sim 2 \times 1\,\mathrm{mm}^2$ at the imaged sample surface, and the latter $\sim 1.5 \times 1.5\,\mathrm{mm}^2$.

Figure 1 shows the schematic of the experimental arrangement used: whilst the master CLASSIX computer controls all aspects of the data acquisition, triggering

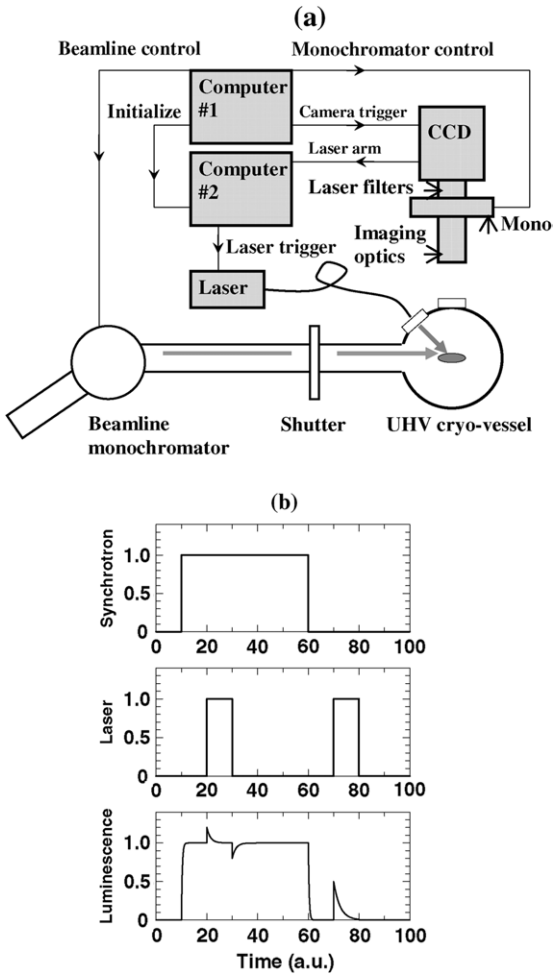

Figure 1. (*a*) Schematic of the experimental arrangement for micro-imaging transient synchrotron–laser luminescence interactions. (*b*) Demonstration of the timing sequences involving both the synchrotron and lasers, as discussed in the text: the synchrotron + laser transients can be repeated and averaged, whereas the laser-only transient is a one-shot signal.

the CCD camera and control of both beamline-excitation and CLASSIX-emission monochromators, a second slave computer is also deployed to control the timing sequence of the laser pulses. The reasoning behind this is that there is a finite time delay between requesting the CCD camera to record data and the actual data recording; more accurate timing is available from a signal sent from the camera that indicates the exact moment of data acquisition. Figure 1 also shows a schematic of the timing sequences involved: averaging of multiple transients is possible when both synchrotron and laser are activated, but luminescence transients can also activated by the laser after the synchrotron light is switched off: as these involve charge de-trapping processes, only a single-shot readout is possible for such events.

A crucial aspect of these measurements concerns the energy range of luminescence photons being detected in relation to both the synchrotron-pump and laser-probe energies. Specifically, it is necessary to discriminate against all luminescence signals that can be stimulated only by the laser in the normal Stokes-shifted energy regime (i.e. emitting at lower energy than that of the laser). As a consequence, additional

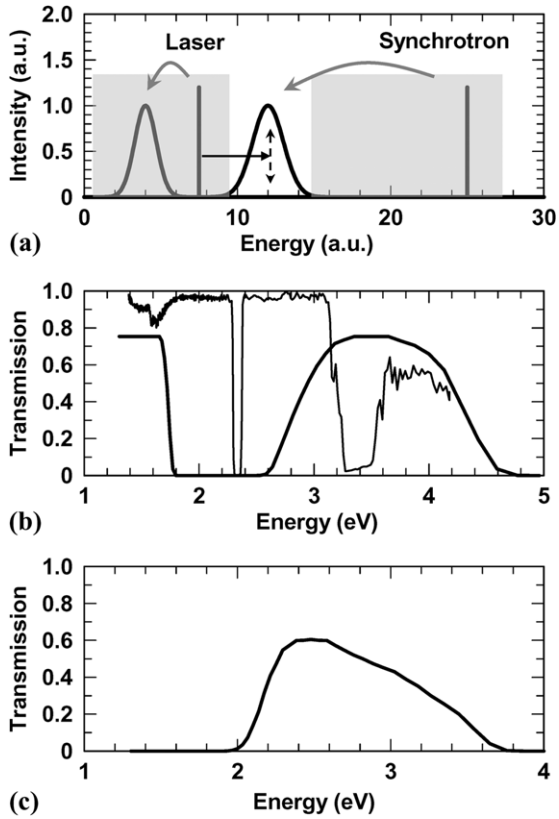

Figure 2. (*a*) Schematic, demonstrating the energy regime for detection: both laser and synchrotron can potentially stimulate luminescence at lower energy. However, the optical window for the experiments is higher in energy than that of the laser, but lower than that of the synchrotron light. This ensures that luminescence stimulated by only the laser is discriminated against, and only laser interactions with the synchrotron-stimulated luminescence are detected (as indicated by the dashed arrow). (*b*), (*c*) Optical transmission windows of the filters used when deploying the 2.33 eV and 1.49 eV lasers, respectively.

optical filtering is introduced to the normal CLASSIX optical arrangement that provides a detection window higher in energy than the laser, but lower than the synchrotron: this ensures that during the synchrotron–laser interactions, only changes induced by the laser on the synchrotron-pumped luminescence are detected (i.e. not ad-mixed with direct laser-stimulated luminescence). In order to effectively remove the laser photons from being detected by the camera, the filter transmission at the laser wavelengths compared with the luminescence transmission window needs to be typically better than $10^{-15}:1$, which represents a significant optical challenge, particularly if a wide detection window is required for spectrally resolving the pump–probe interactions. Laser-rejection filter combinations are shown in figures 2(*b*) and (*c*) which were successfully deployed for the 2.33 eV (532 nm) and 1.49 eV (830 nm) lasers, respectively. For the 2.33 eV laser, a useful broad detection window in the range 2.6–4.5 eV is possible using standard Schott BG3 colour-glass filters, but this is inadequate for laser rejection even if substantially thicker filters were to be deployed than the 3 mm used here: effective laser rejection was possible however, by the additional use of two 2.33 eV notch filters (Semrock; NF01-532U), providing an additional optical density of 10 at the laser energy: these interference filters have the added benefit of minimizing laser-induced fluorescence of the colour-glass filters. Rejection of the 1.49 eV laser light was substantially easier, with 6mm standard Schott BG39 colour glass providing the necessary filtering directly, whilst providing a wide detection window from 2.1 to 3.6 eV for further monochromatic analysis of the pump-probe signals.

3. Example results

In the following sections, example results from heterogeneous alumino-silicate samples are provided. There are two reasons for choosing such systems for study: firstly, the naturally occurring crystals provide an ideal case study for comparing the chemical and defect distributions on the mesoscopic scale analysable with CLASSIX. However, the second and more general reason is that such samples are widely used as natural radiation dosimeters for geological and archaeological dating applications, and knowledge about the distribution of radiative and non-radiative centres within the materials is crucial in order to understand issues such as charge loss due to tunnelling between radiative and non-radiative defect sites (e.g. Huntley 2006) which can have a serious impact on retrospective dose evaluation.

3.1. Correlating the bulk sample chemistry with radiative defect distributions

Before considering the more complex case of mapping pump–probe interactions, the more simple case of the correlation of radiative defect sites with the crystal chemistry is considered. The sample used in the study has a bulk composition of $(KNa)AlSi_3O_8$ (measured using microprobe analysis) but, having been cooled slowly from the melt, has segregated into zones richer in $KAlSi_3O_8$ and $NaAlSi_3O_8$, respectively, providing a naturally occurring 'super-lattice' structure: the band-gaps of the two crystal types are 7.7 and 7.86 eV respectively (Malins *et al* 2004). The luminescence emission characteristics of this sample are, however, quite striking. Both crystal structures commonly display both red and blue emissions relating to the point defects Fe^{3+} (extrinsic) and [Al–O^-–Al] (intrinsic) (Krbetschek *et al* 1997), but as shown in figure 3, these defects are almost exclusively associated with the sample zones richer in Na and K, respectively. In the case of the extrinsic defect Fe^{3+}, the conclusion is that during the slow cooling of the crystal where the mobility of the K and Na ions has led to phase segregation, the Fe^{3+} ions have also preferentially migrated to the Na-rich zones; even within these regions, there is significant variation in the Fe^{3+} concentrations. It is also clear that the formation of the intrinsic [Al–O^-–Al] defects is more energetically favourable in $KAlSi_3O_8$ than in $NaAlSi_3O_8$.

Superficially, the comparison of the chemical and luminescence maps shown for the present example in figure 3 could equally have been achieved via electron microprobe analysis with energy-resolved luminescence emission detection capability. The use of CLASSIX, however, provides a number of general advantages: (i) because the x-ray absorption features are spectrally resolvable, details of the structural environment (including crystal field splitting of the *L*-edges observed here), or full EXAFS analysis

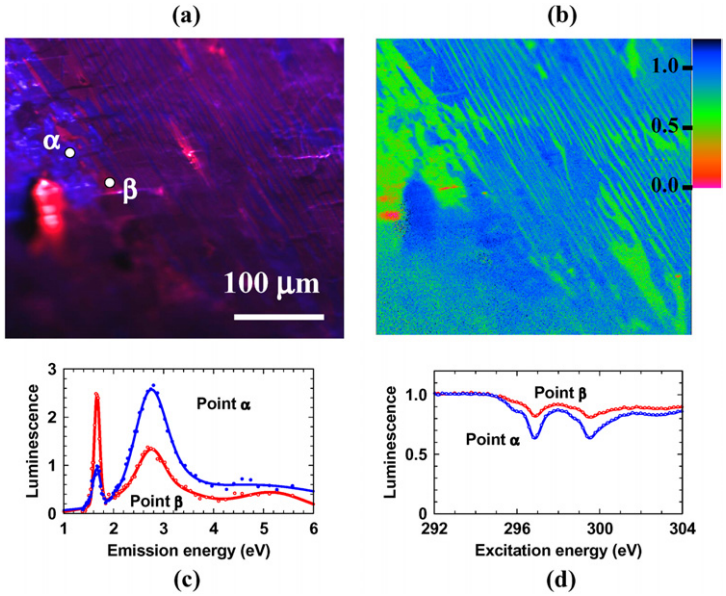

Figure 3. (*a*) Composite micro-image of the synchrotron-stimulated luminescence in a phase-exsolved sample of (K,Na)$AlSi_3O_8$, taken at 1.68 eV (red) and 3 eV (blue). (*b*) Comparative chemical map, showing the distribution of K (green) within the sample obtained by mapping the $L_{2,3}$-edge ODXAS: the scale references the normalized luminescence at L_3. (*c*) Full emission spectra recorded at the points indicated; 292 eV excitation energy. (*d*) Full excitation spectra at the points indicated, taken when scanning across the K $L_{2,3}$ core levels. $T = 40$ K.

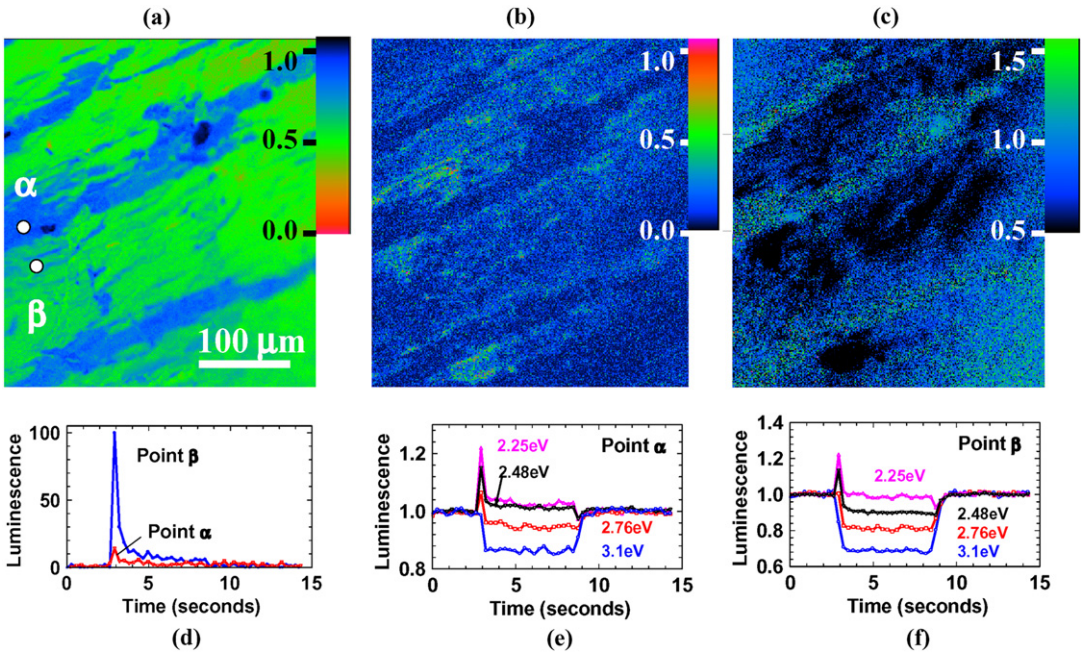

Figure 4. (*a*) Map showing the distribution of K (green) in a phase-exsolved sample of (KNa)$AlSi_3O_8$ obtained by mapping the $L_{2,3}$-edge ODXAS: the scale references the normalized luminescence at L_3. (*b*) Comparative map of the temporal laser-stimulated luminescence obtained *after* the synchrotron exposure has ceased. The map shows where the de-trapping of charge from the *non-radiative* centres occurs (seen here as bright). (*c*) Comparative map showing quenching of synchrotron-induced luminescence (see here as dark) caused by the *simultaneous* additional application of the laser. The scale references the normalized luminescence intensity of the synchrotron-only luminescence intensity. (*d*) Temporal variation of the laser-only de-trapping luminescence at the points indicated: laser 'on' at $T = 2.5$ s; laser 'off' at 8.5 s. (*e*), (*f*) Temporal variation of the synchrotron-laser interactions at the points indicated, at a variety of emission detection energies. The synchrotron 'on' during the whole scan: laser 'on' at $T = 2.5$ s; laser 'off' at 8.5 s. $T = 40$ K.

are obtainable directly from the luminescence signatures; (ii) microprobe analysis relies on electron excitation which cannot be used in all circumstance (e.g. high pressure applications), whereas CLASSIX is an all-photon system more amenable to deployment in adverse experimental environments; (iii) whilst an electron microprobe provides a measure of a sample's chemistry averaged over the volume of the electron bulb, ODXAS provides the chemistry and structure of the sample typically within a few Ångstroms of the point of luminescence emission; (iv) the use of an electron microprobe

excludes the possibility for energy-resolved pump–probe measurements.

3.2. Micro-imaging synchrotron–laser interactions

In order to demonstrate the value of mapping synchrotron–laser interactions, a similar sample to that described in section 3.1 is used, again with bulk composition $(KNa)AlSi_3O_8$, phase segregated into zones of materials richer in $KAlSi_3O_8$ or $NaAlSi_3O_8$: figure 4(*a*) shows the chemical distribution of K in the material, obtained by mapping the *L*-edges via ODXAS. Two main interactions with laser light are possible, as demonstrated schematically in figure 5. During exposure to the synchrotron ionizing radiation, luminescence can result from the recombination of charge at radiative centres, but this is in competition with electron capture at deep-lying non-radiative defects. During synchrotron irradiation, the simultaneous application of laser light can lead to two important effects. Firstly, it can serve to de-populate the non-radiative centres (the process indicated by 'Laser 1' in figure 5), yielding enhanced luminescence at the radiative recombination centres. However, the presence of the non-radiative defects can also be detected post-synchrotron exposure by laser de-trapping of accumulated charge, which yields a temporal burst of luminescence whilst the laser remains active, lasting until charge de-trapping is complete. During simultaneous synchrotron–laser interaction, the application of the laser also results in this temporal luminescence burst, but the final equilibrium luminescence level is usually different from the synchrotron-only luminescence equilibrium, due to the changed population of the non-radiative trapping sites. (Normally, this at an enhanced level, though this depends on the details of the defect populations and relative trapping rates.) The second form of laser interaction is via direct competition with charge filling of the radiative recombination centres during synchrotron radiation (the process indicated by 'Laser 2' in figure 5): this is normally expected to yield quenching of the observed luminescence, though the degree of quenching again is dependent on the relative capture cross-sections of the hole with synchrotron-derived electrons in the conduction band, and laser-excited electrons from the valence band. (Naturally, for the latter to occur, the laser energy must be at or above the photo-ionization threshold of the defect.)

The maps provided in figure 4 allow a comparison to be made of the 1.49 eV laser interactions involving radiative and non-radiative centres, with the chemical distribution of K in the bulk lattice. Figure 4(*b*) captures the moment of maximum charge release from the non-radiative centres during laser exposure post-synchrotron exposure, thereby providing direct evidence of the distribution of these defects. What is immediately apparent is that the defects are principally located within the K-rich zones of the phase-exsolved lattice, but that their distribution is preferentially located close to the boundaries with the Na-rich zones. In comparison, the CW synchrotron-laser interaction that leads to quenching of the luminescence via direct competition with the main recombination sites is also primarily located within the K-rich zones (figure 4(*c*); dark areas). Their distribution is however significantly different, being more ubiquitously distributed throughout the lattice.

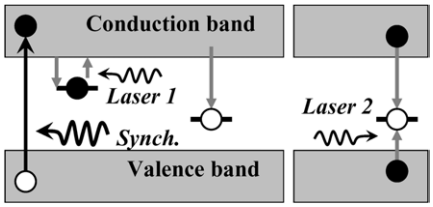

Figure 5. Schematic of the main interactions of the laser with charge-trapping defects within the material. The synchrotron acts as a luminescence pump, promoting electrons into the conduction band from the valence band (or atomic core levels) which can subsequently recombine radiatively at hole-trapping centres. The simultaneous application of a laser can interact directly with these recombination centres (as shown by process 'Laser 2'), normally resulting in quenched luminescence. If there are also traps present that compete non-radiatively for the synchrotron-stimulated electrons, the laser probe can also interact with these defects (as shown by process 'Laser 1') and this usually results in enhanced luminescence emission at the radiative sites.

Details of the temporal variation of the signals are provided in figure 4(*d*) for the de-trapping luminescence at points (α, β), and in figure 4(*e*) and (*f*) for the synchrotron–laser interactions. From the latter, it is clear that the signals depend strongly on the emission wavelength chosen: at 3.1 eV (400 nm) for example, the interactions are primarily with the recombination centre, almost certainly due to the laser energy being close to the trap depth from the valence band. In contrast, if an emission window at 2.25 eV (550 nm) is chosen, there appears to be no interaction with the recombination centre, and all the transient signals are driven by the non-radiative centres. Here, the positive signal on application of the laser is due to de-trapping of charge built up during the previous synchrotron exposure, and the negative transient signal on removal of the laser is due to increased competition involving the now charge-depleted non-radiative centres. (Once these centres are saturated, their competition reduces to zero.)

4. Summary and future directions

A method has been described that allows the micro-imaging of synchrotron–laser interactions in luminescent materials: in the examples given involving heterogeneous silicates, mapping of the distributions of both radiative and non-radiative trapping sites has been possible, with direct correlation to the sample chemistry. The measurements are strongly dependant on the emission wavelengths chosen for study, and extending them to fully tuneable laser sources would offer the additional possibility for direct determination of the electronic energies of non-radiative defects present. Because all-optical detection is used, the sensitivity of the measurements is very high; nevertheless, undertaking measurements on third generation synchrotron sources (rather than the second generation SRS Daresbury, as described here) would significantly expand the range of interactions that can be probed, and kinetic range of the signals that can be studied.

Acknowledgments

This work has been made possible by funding from EPSRC (grant award EP/C511212/1) and by CCLRC for the provision of beamtime, award reference 46058. We are grateful to Dr Ole Johnsen of Copenhagen University for the loan of the silicate samples used in the work, and for undertaking the electron microprobe analyses.

References

Bowler M, West J B, Quinn F M, Holland D M P, Fell B, Hatherley P A, Humphrey I, Flavell W R and Hamilton B 2002 *Surf. Rev. Lett.* **9** 577–81

Dalba G, Daldosso N, Fornasini P, Grimaldi M, Grisenti R and Rocca F 2000 *Phys. Rev.* B **62** 9911–14

Emura S, Moriga T, Takizawa J, Nombra M, Bauchspeiss K R, Murata T, Harada K and Maeda H 1993 *Phys. Rev.* B **47** 6918–30

Huntley D J 2006 *J. Phys.: Condens. Matter* **18** 1359–65

Krbetschek M R, Götze J, Dietrich A and Trautmann T 1997 *Radiat. Meas.* **27** 695–748

Malins A E R, Poolton N R J, Quinn F M, Johnsen O and Denby P M 2004 *J. Phys. D: Appl. Phys.* **37** 1439–50

Poolton N R J, Hamilton B and Evans D A 2005 *J. Phys. D: Appl. Phys.* **38** 1478–84

Poolton N R J, Towlson B M and Hamilton B 2006a *Nucl. Instrum. Methods* B **246** 445–51

Poolton N R J, Towlson B M, Evans D A and Hamilton B 2006b *New J. Phys.* **8** 76

Soderholm L, Liu G K, Antonio M R and Lytle F W 1998 *J. Chem. Phys.* **109** 6745–52